Brazilian Journal of Physics (2023) 53:158
https://doi.org/10.1007/s13538-023-01371-0

SOCIEDADE BRASILEIRA DE FÍSICA

CONDENSED MATTER

Synthesis by Mechanical Alloying and Characterization $Fe_{73}Si_{22}B_5$ Alloy: Amorphization Evaluation

Luciano Nascimento[1] · **Ana Cristina Figueiredo de Melo Costa**[1]

Received: 20 July 2023 / Accepted: 29 September 2023 / Published online: 18 October 2023
© The Author(s) under exclusive licence to Sociedade Brasileira de Física 2023

Abstract
This work synthesized and investigated the amorphous alloy $Fe_{73}Si_{22}B_5$ obtained by high-energy milling. The properties of the amorphous alloy $Fe_{73}Si_{22}B_5$ were investigated by X-ray diffraction (XRD), scanning electron microscopy (SEM) with EDS, Fourier transform infrared spectrometry (FTIR), thermal analysis TGA/DTA, textural analysis by N2 (BET/BJH), and magnetic measurements (VSM). The results confirmed that the $Fe_{73}Si_{22}B_5$ alloy reached the desired amorphization degree and presented IV isotherms with a hysteresis loop for mesoporous materials. The TGA/DTA confirmed that Fe and Si ions are quickly oxidized in the environment with the mass slightly increased to 27.5%. The $Fe_{73}Si_{22}B_5$ exhibited soft magnetic properties with ferromagnetic characteristics. The FTIR spectra exhibit absorption peaks corresponding to the presence of (R)O–H, Fe–O, Si–O, O–Fe–O, and Si–O–Fe groups. This result suggests that the developed high-performance $Fe_{73}Si_{22}B_5$ amorphous alloy has great application potential in various research fields.

Keywords Amorphous alloy $Fe_{73}Si_{22}B_5$ · Amorphization · Mechanical alloying (MA)

1 Introduction

Since their discovery in 1960, amorphous alloys have been widely studied, and even after five decades, their potential has yet to be fully revealed. Starting from a binary alloy, $Au_{75}Si_{25}$ was reported by Duwez and collaborators; they developed a rapid solidification technique, melt spinning, with a cooling rate of the order of 10^5–10^6 Ks^{-1}, showing that the process of nucleation and growth of the crystalline phase could be kinetically avoided in some alloys, and thus, the configuration of atomic structure of the liquid metal would be maintained, resulting in a metallic glass [1, 2]. In addition to the scientific significance of understanding the nature of the Au–Si system, it is most puzzling due to its high complexity. The Au–Si system recently received significant attention because of its technological importance, including the growth and self-assembly of Si nanowires, interconnections of Si-based electronic devices, and bonding of nanoelectromechanical devices [3].

Various synthesis methods were reported for the Au–Si and other amorphous alloy systems; for example, rapid solidification (RSP) and powder metallurgy (PM) have been widely used to obtain these alloys and have great direct scientific and commercial applications [4, 5]. Fe-based amorphous alloys are thermodynamically metastable and structurally characterized by long-range disordered atomic arrangements without grain boundary, crystal segregation, and defects that cannot be observed in other conventional crystalline alloys [6]. Moreover, Fe-based amorphous alloys have practical applications in various industry sectors due to their exhibiting good soft magnetic properties, good mechanical behavior (have a tensile strength limit of 840–2100 Mpa [7] combined with a Young's modulus of 47–102 Gpa [8] as well as a high Vickers hardness value [9]), and high corrosion resistance in saline environments [10].

The $Fe_{78}Si_{13}B_9$ amorphous alloy was commercially used as a core material in high-power electrical transformers [11]. The Fe–Si–B alloy series are class of alloys widely used and available today due to their much lower coercivity (H_c) in the range of 2.2–4.3 A/m and have high permeability

✉ Luciano Nascimento
luciano.uepb@gmail.com

Ana Cristina Figueiredo de Melo Costa
ana.costa@ufcg.edu.br

[1] Federal University of Campina Grande-UFCG, Academic Unit of Materials Engineering, Laboratory of Synthesis of Ceramic Materials – LabSMaC, Av. Aprígio Veloso, 882 - Bodocongó, 58429-900 Campina Grande, PB, Brazil

($\mu_e = 8.8–12.8 \cdot 10^3$) [12], high saturation magnetization (M_s) in the range 1.53–1.68 T [13, 14], higher electrical resistivity of $\rho = 1.0 \sim 1.3$ μΩm [15], and lower core losses compared with silicon steels ($FeSi_{75}$), because the Fe–Si–B amorphous alloys possess six times fewer energy losses than traditional Fe–Si alloys at industrial frequencies [16, 17]. The amorphous alloy $Fe_{79}B_{13}Si_8$ has a higher Curie temperature without changing core losses and flux density compared with Fe_3Si alloys in the fabrication of power transformers.

Therefore, $FeSi_{75}$ alloys are traditionally used in various in high-frequency applications in industrial sectors [18, 19]. Another promising application of these materials concerns exploiting their magnetoelastic properties to be used in sensors and biosensors in biomaterials [20, 21]. The effect of metalloids in Fe-based amorphous alloy formation (typically B, Si, Te, As, Sb, and the use of C or P) plays a crucial role in the soft magnetic properties, thermal stability, and mechanic concerning the amorphization of its phases [13, 22]. Solid-state amorphization offers another method for producing amorphous alloys, for example: melt spinning [23], gas atomization [24], mechanical alloying/milling [25], copper die casting [26], chemical vapor deposition (CVD) [27], plasma treatment [28], plasma chemistry [29], and other varieties of metallurgical process techniques.

Amorphization in mechanical milling is associated with the interdiffusion of constituent elements and with lattice defects introduced by mechanical stresses, resulting in a metastable state when milling is conducted below the glass transition temperature [30]. By incorporating these lattice defects, it has been suggested that amorphization by process mechanical alloying (MA) is possible when the free energy of the crystalline phase can be increased to a higher level in the amorphous phase [31, 32]. Process mechanical alloying (MA) involves solid-state reactions with amorphous powders, requiring repeated cold welding, crushing, and rewelding of the mixed powders in a high-energy ball mill [33]. Mechanical alloying (MA) can synthesize various equilibrium and non-equilibrium alloy phases, starting from blended elemental or pre-alloyed powders [34].

The non-equilibrium phases synthesized include supersaturated solid solutions, metastable crystalline and quasicrystalline phases, nanostructures, and amorphous alloys [35]. Recent advances in disordering and ordered intermetallics in the mechanochemical synthesis of materials have been done after discussing process variables involved in MA [36]. In this context, this paper reports the preparation of $Fe_{73}Si_{22}B_5$ alloy, evidenced by the powder amorphization by mechanical alloying route with a milling time of 10 h. To this end, structural, thermal, magnetic, and morphological analyses were investigated. The milling time of 10 h required for $Fe_{73}Si_{22}B_5$ alloy amorphization state for its morphological and microstructural evolution of the powders, thermal stability exhibited good soft magnetic properties, and an estimate of the specific surface area of the alloy powder $Fe_{73}Si_{22}B_5$ with type IV isotherm with hysteresis loop type H3, with characteristics of mesoporous materials, was presented and discussed, respectively.

2 Experimental Procedures

The nominal composition of the amorphous alloy $Fe_{73}Si_{22}B_5$ (at. %) obtained from mixtures of pure crystalline powders of Fe (99.99%, 50 μm), Si (99.99%, 40 μm), and B (99.99%, 30 μm) purchased from Brazil — Sigma-Aldrich. During the processing of the alloy $Fe_{73}Si_{22}B_5$, no periodic collection was performed. The powders weighed on a BK4000 Micronal balance with a resolution of 10^{-2} g of the chemical elements in the proportions corresponding to the nominal composition $Fe_{73}Si_{22}B_5$. Mechanical alloying was performed in a high-energy planetarium (Fritsch Pulverisette 5) used with cylindrical jars of 77 mm diameter for 80 mm tall and spheres (20, 12, and 7 mm in diameter), both of which are tungsten spheres and jars. The charge of the powder mixture was maintained at 20 g for all tests, as well as the ball-to-powder weight ratio of 10:1.

The test speed adopted was 250 rpm, and the grinding time was 10 h. Finally, *n*-hexane (C_6H_{14}) (2 mL) was used as a grinding medium and argon atmosphere. The *n*-hexane (C_6H_{14}) used as a process control agent (PCA) was purchased from Hexis Scientifics/Brazil. With the purpose of adhesion of ductile particle powders of the alloy $Fe_{73}Si_{22}B_5$ by cold welding between the spheres and the jar wall, we use *n*-hexane (C_6H_{14}) as a process control agent (PCA) for the morphology of the homogenized powder in the alloying process and an argon atmosphere to prevent further oxidation of the metal powders. The grinding of metallic powders was carried out at an ambient temperature between 20 ºC and 25 °C, with 25 °C being the most mentioned. Mixing the mechanically bonded powders produced an amorphous structure within 10 h of milling.

The analysis of the amorphous structure was performed by X-ray diffraction (XRD) with a BRUKER diffractometer, model D2 Phaser, by copper radiation $CuK_{\alpha 1}$ ($\lambda = 1{,}40{,}621$ Å) and $CuK_{\alpha 2}$ ($\lambda = 1{,}54{,}439$ Å), 0.016 s^{-1} sweep step, and a time of 5 s, at 40 kV and 30 mA in 2θ ranging from $10º \leq 2\theta \leq 80º$. The VEGA-TESCAN TS5130LSH (Oxford Instruments) field-emission-gun scanning electron microscope (SEM) equipped with energy-dispersive X-ray spectroscopy (EDS) was used to characterize the morphological aspect microstructure and elemental composition of amorphous alloy powder $Fe_{73}Si_{22}B_5$. Quantitative EDS analysis was performed using the INCA Micro Analysis Kit from Oxford Instruments and the X-Max 20 SDD detector. It operates with a tungsten filament in the range of 200 V–30 keV with an emission probe current of 300 mA.

Magnification range is 3–10,000 × with the spatial resolution down to 3 nm.

The amorphous alloy $Fe_{73}Si_{22}B_5$ used for SEM/EDS microstructural characterization was prepared using standard metallography with gold. The absorption spectrum for the $Fe_{73}Si_{22}B5$ amorphous alloy was recorded on a Fourier transform infrared spectrophotometer (Bruker model TENSOR 27) from 3000 to 500 cm^{-1}, respectively. Thermogravimetric analysis (TGA/DTA) of the amorphous alloy $Fe_{73}Si_{22}B_5$ was performed in an analyzer thermostat, SHIMADZU brand, model DTG-60H, with rate heating time of 10 ºC min^{-1}, starting the analysis at over a temperature range ranging from ambient to 1000 ºC, using a nitrogen atmosphere with a gas flow of 50 mL min^{-1} and 10 mg of sample in an alumina crucible. The textural analysis was carried out in a Quantachrome surface area and pore size analyzer, model Autosorb IQ, where the adsorption/desorption isotherms of the amorphous alloy $Fe_{73}Si_{22}B_5$ were obtained. Magnetic measurements were obtained using a vibrating sample magnetometer (Microsense model EZ 7 Vibrant Sample Magnetometer (VSM)) subjected to magnetic fields up to 2.7 T (i.e., 27 kOe) and at temperatures in the temperature range of 77 to 1000 K. The field magnetization was parallel to the length of the sample to minimize the demagnetization effect. The magnetization curves were analyzed by the least squares method. The coercive force H_c of the rods was investigated using a coercimeter with a permalloy probe.

3 Result and Discussions

Figure 1 shows the XRD pattern of the wet mechanical milling powder in the $Fe_{73}Si_{22}B_5$ alloy from 10 h of milling displayed in the 2θ range of 40º–50º around ($2\theta = 44$º), presenting a typical diffuse halo peak, and no sharp diffraction peaks corresponding to the crystalline phases, implying a fully amorphous structure in the composition of $Fe_{73}Si_{22}B_5$ indicated inside the red circle.

Due to the small amount of B and its amorphous state, no signal from this phase can be noticed in the diffraction pattern of the $Fe_{73}Si_{22}B_5$ alloy. Figure 2 shows the micrograph of the SEM/EDS of the alloy $Fe_{73}Si_{22}B_5$ obtained during 10 h of milling, with an aggregate of small irregular particles with a small spherical format of a typical size of 50 µm.

On the left side of the SEM micrograph, we observe (see Fig. 2) small irregular spherical particles with a size of 50 µm; particles milled during 10 h of ball milling suffered severe deformation coupled with fragmentation–aggregation that the powder particles were trapped between the colliding balls due to significant degree of plastic deformation on the complex physicochemical process from the attachment and binding of particles, known as cold welding, and it was observed for powder/powder and powder/ball surfaces as well. Already on the right side, we observe the EDS spectrum (see Fig. 2) of the surface of the $Fe_{73}Si_{22}B_5$ powder of a small part of the surface chosen for analysis, with the spectrum peaks of the most intense chemical elements such as Fe and Si relatively evenly distributed in the analysis area. The distribution of B is relatively small compared to the other chemical elements Fe and Si, where both exist in the formation of dilute phases of Fe_3Si and Fe_2B in the $Fe_{73}Si_{22}B_5$ alloy [37]. These phases can be explained by the uniform distribution of Fe_3Si and Fe_2B phases at 10 h of milling of $Fe_{73}Si_{22}B_5$ alloy powder [38]. These reactions occur because the B atom diffuses with the Si atom very slowly during the mechanical milling of the $Fe_{73}Si_{22}B_5$ alloy [39]. Also, at magnification of 100 k × of the micrographs from the SEM, we can observe the larger particles formed by the agglomeration of the smaller particles, which are cold welding and re-welding occurring during the mechanical milling powder process.

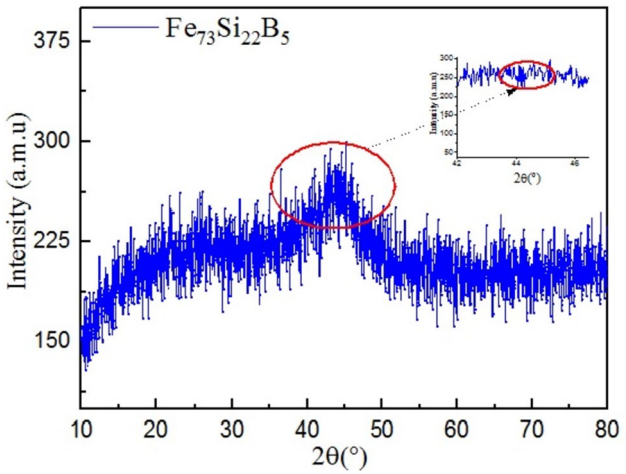

Fig. 1 XRD pattern of $Fe_{73}Si_{22}B_5$ alloy powder

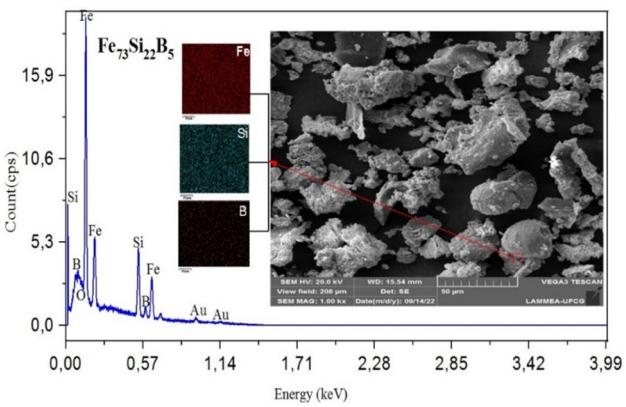

Fig. 2 SEM/EDS micrographs of the alloy $Fe_{73}Si_{22}B_5$

Figure 3 shows the vibrational spectra of the amorphous alloy $Fe_{73}Si_{22}B_5$ obtained by mechanical alloying during 10 h of milling in the infrared region of 3000–500 cm^{-1}.

The observed absorption band at 2338 cm^{-1} corresponds to the presence of (*R*)O–H groups (*R* = Si and B or Ba…), e.g., silanol group SiOH [40]. A broad absorption band observed in the region of 2104 cm^{-1} corresponds to the stretching mode characteristic in the Si–O [41]. The appearing absorption band around 1992 cm^{-1} corresponds to the O–Fe–O bending mode [42]. The absorption band at 638 cm^{-1} represents the stretching vibration of the Fe–O bond in Fe_3O_4 [43]. The occurrence of an absorption band at 592 cm^{-1} indicates the presence of Si–O–Fe [44].

Figure 4 shows the thermal events observed from the superimposed curves of TGA/DTA of the alloy $Fe_{73}Si_{22}B_5$ obtained by mechanical alloying during 10-h milling.

The amorphous $Fe_{73}Si_{22}B_5$ alloy thermal stability measurement was carried out using TGA, as shown in Fig. 4. The temperature range from ambient temperature to 1000 ºC was measured in a nitrogen environment at a scanning rate of 10 °C min^{-1}. A small exothermic peak can be observed at 32.82–388.55 °C where there is a significant mass loss of ~ 96.17% being attributed to the transformation of the remaining amorphous phase to a metastable phase. In the DTA curve for the amorphous alloy $Fe_{73}Si_{22}B_5$, we observe an exothermic peak at the maximum temperature of $T_x = 505$ ºC for the ground powder during the 10 h of mechanical milling, respectively. The glass transition temperature $T_g = 458.55$ ºC, crystallization start temperature $T_x = 505$ ºC, and corresponding supercooled liquid region ($\Delta T = T_x - T_g = 46.45$ ºC) from the endothermic peak were used to evaluate the glass-forming ability (GFA) for bulk metallic glasses (BMGs) [45]. Slight weight loss (0.16%) was obtained from TGA measurement due to evaporation from moisture absorption.

With the increase in temperature, which varies between 100 and 993.22 ºC, it was observed that the environment oxidizes the Fe and Si ions. Consequently, the total mass was slightly increased to 27.5% (see Fig. 4 due to that the increased grain size relative to the ionic radius of the Fe (0,55 Å) is much larger than the ionic radius of Si (0,26 Å)) [46, 47]. Therefore, a great total mass slightly increased to 27.5% is observed on the curve, reflecting a paramagnetic-to-ferromagnetic transition [48]. TGA results from the $Fe_{73}Si_{22}B_5$ alloy indicate the formation of several complex ordered crystals diluted with the amorphous phase. These crystals may be deduced to form in the compound by a mixture of three phases: Fe_2B, Fe_3Si, and a little α-Fe phase in the temperature range of 87.99–924.7 °C, with equilibrium phase stabilization at high temperatures [49, 50].

Figure 5 shows the adsorption/desorption isotherms of N_2 at 77 K for the $Fe_{73}Si_{22}B_5$ alloy during 10-h milling. The hysteresis loops of the black and red lines represent the adsorption curves (ADS) and desorption (DES).

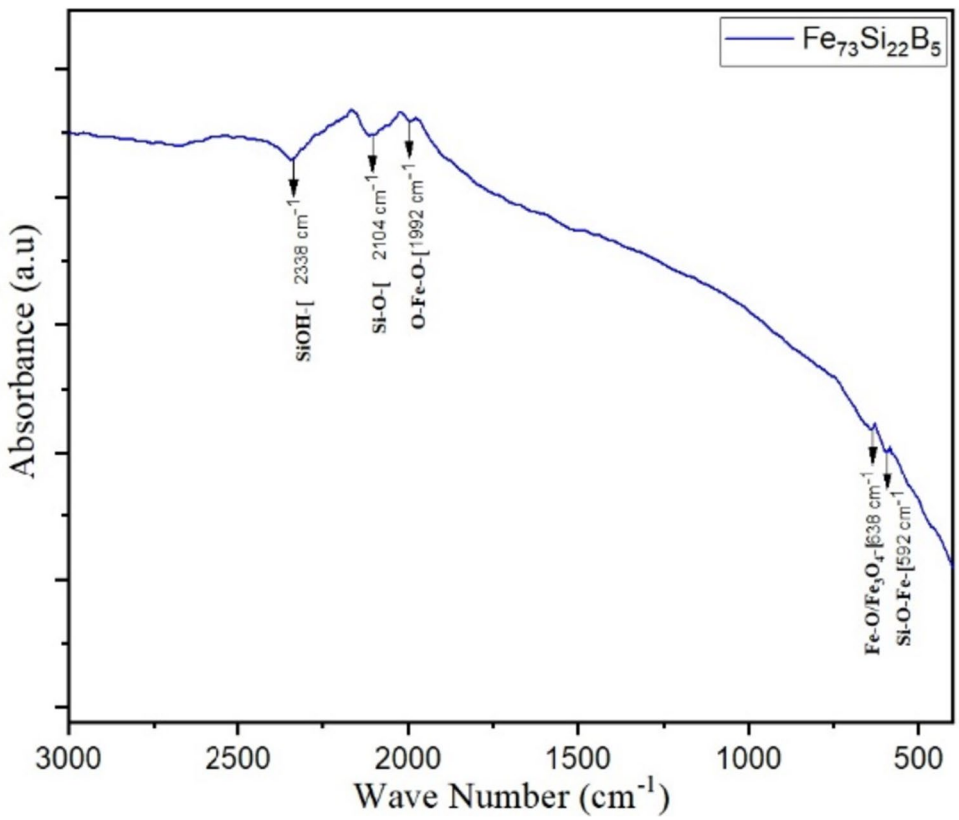

Fig. 3 FTIR spectrum of the $Fe_{73}Si_{22}B_5$ alloy in the region of 3000–500 cm^{-1}

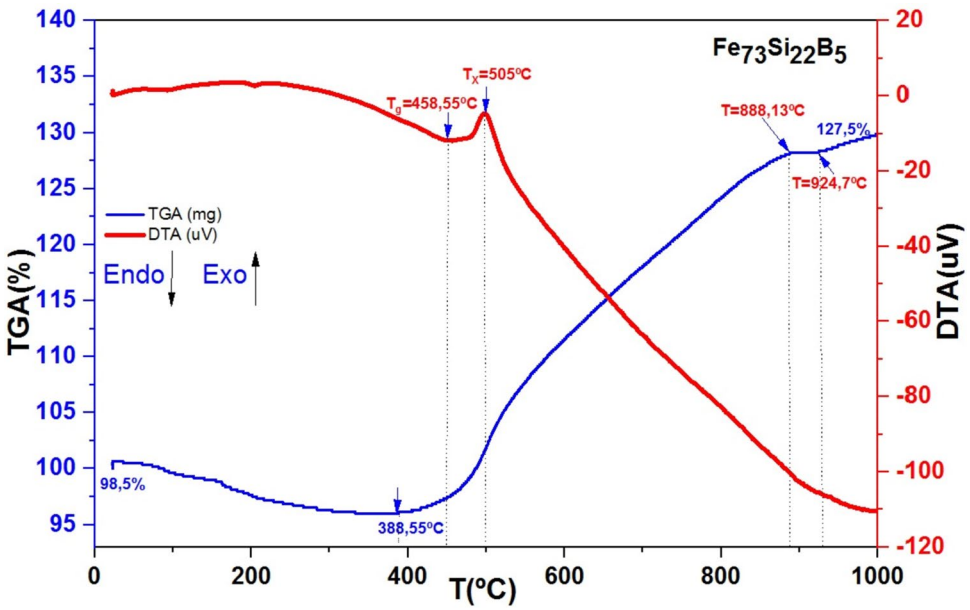

Fig. 4 Overlapping TGA/DTA curves of the alloy $Fe_{73}Si_{22}B_5$

N_2 adsorption-desorption isotherms were performed to estimate the specific surface area of $Fe_{73}Si_{22}B_5$ alloy powder and type IV isotherm with hysteresis loop profile characteristic of type H3 [51], as illustrated in Fig. 5. Through the Brunauer-Emmett-Teller (BET) method, the specific surface area was determined to be about 0.271 $m^2\ g^{-1}$. Thus, the amorphous alloy $Fe_{73}Si_{22}B_5$ has an estimated pore volume of 0.0226 $cm^3\ g^{-1}$, being characterized as a mesoporous material. As shown in Fig. 5, a typical isotherm of a mesoporous solid is observed, characterized by a very pronounced hysteresis loop between the adsorption and desorption branches for $Fe_{73}Si_{22}B_5$ alloy [52]. It is observed that the isotherms of the amorphous alloy $Fe_{73}Si_{22}B_5$ in Fig. 5 show a hysteresis inflection point close to $P/P_o = 0.4 - 1$, being characterized by a high mesoporosity and presenting an adsorption and desorption cycle in the $P/P_o = 0.8 - 1$ range, being related to a macropore phase.

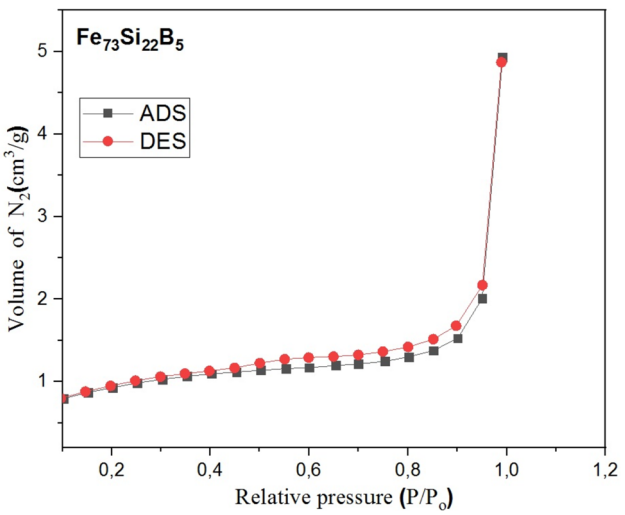

Fig. 5 N_2 adsorption/desorption isotherms for the $Fe_{73}Si_{22}B_5$ alloy

Figure 6 shows the hysteresis loops M–H for the $Fe_{73}Si_{22}B_5$ alloy, which is typical of soft magnetic ferromagnetic materials.

Hysteresis loop M–H of amorphous alloy $Fe_{73}Si_{22}B_5$ is the estimated value of saturation magnetization $M_s = 15{,}003$ emu/g, remanent magnetization $M_r = 0.0122$ emu/g and a coercive field of $H_c = 77.82$ kOe, respectively. In the upper part of Fig. 6, we can observe the strong presence of the ferromagnetic properties property of the amorphous alloy powder $Fe_{73}Si_{22}B_5$ obtained by mechanical alloying (MA) during the 10 h from the milling powder [53].

In addition, the illustration in the lower right corner of Fig. 6 also shows that its field coercivity has a tendency to decrease. The amorphous alloy $Fe_{73}Si_{22}B_5$ exhibits the highest $M_s = 15{,}003$ emu/g value, which is attributed to the highest Fe and Si content and the lowest B content. One can clearly see an absence of magnetocrystalline anisotropy due to the existence of amorphous phases [54]. Obviously, the value of $M_s = 15{,}003$ emu/g depends on the time 10 h of milling [55]. With the prolongation of the milling time, the volume fraction of α-Fe phase precipitation diluted in the amorphous phase increases gradually, resulting in a greater increase in the value of its saturation magnetization and indicating superior soft magnetic properties [56, 57]. The increase in the saturation magnetization of $M_s = 15{,}003$ emu/g in the case of the amorphous alloy $Fe_{73}Si_{22}B_5$ from the ground powder for 10 h can be attributed to the amorphization of the powder and the decrease

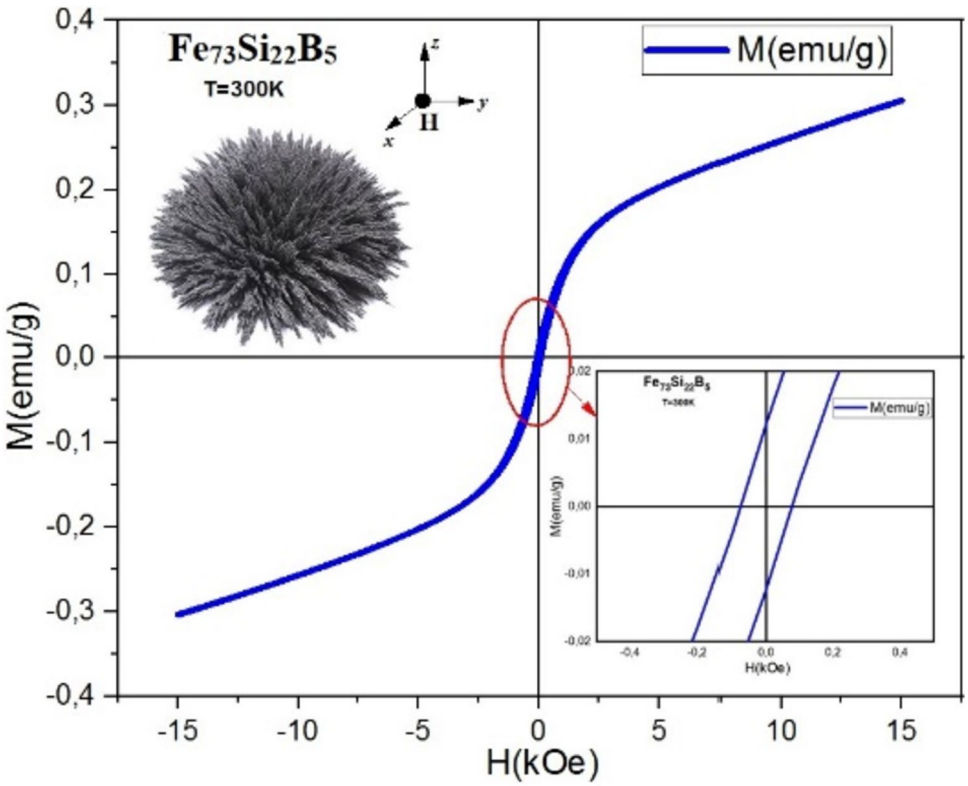

Fig. 6 Hysteresis loop M–H for the $Fe_{73}Si_{22}B_5$ alloy

in the size of the morphology of irregular crystallites and small spheres.

4 Conclusion

X-ray diffraction analysis showed the formation from a diffuse halo around 2θ = 44º exhibiting the shape of an amorphous structure and its evolution in milled powder $Fe_{73}Si_{22}B_5$ alloy by 10 h through mechanical alloying. The SEM/EDS micrograph of the $Fe_{73}Si_{22}B_5$ alloy powder showed the morphology of small irregular particles and small spheres with a typical size of 50 µm, where the predominance of Fe and Si is distributed uniformly on the surface area. The thermal events that were observed from the superimposed curves of TGA/DTA for the amorphous alloy $Fe_{73}Si_{22}B_5$ in the temperature range between 100-993. 22°C, showed a total mass gain of 27.5%, and presented an exothermic peak in glass transition temperature (Tg = 458. 55 °C) and with its first crystallization temperature that is around (Tx = 505 °C). The TGA results show a 27.5% mass increase due to the oxidation of Fe and Si ions by the environment.

Hence, the mass could be slightly enhanced to 27, 5%, due to the ionic radius of Fe (0,55 Å) being much larger than the ionic radius of Si (0.26 Å). In the FTIR analysis of the $Fe_{73}Si_{22}B_5$ powder, the absorption peaks corresponded to the presence of (*R*)O–H, Fe–O, Si–O, O–Fe–O, and Si–O–Fe groups. The N_2 adsorption-desorption isotherms of the $Fe_{73}Si_{22}B_5$ alloy present a type IV isotherm with a hysteresis loop profile characteristic of type H3 for mesoporous materials; it was also verified estimated value of saturation magnetization of $M_s = 15{,}003$ emu/g, remanent magnetization $M_r = 0.0122$ emu/g, and a coercive field of $H_c = 77{,}82$ kOe, for a ferromagnetic material, featuring superior soft magnetic properties and expected to have attractive application prospect.

Author Contribution Luciano Nascimento: Experiment, analysis and paper writing. Ana Cristina Figueiredo de Melo Costa: Conceptualization, analysis and supervision.

Funding The authors wish to thank CAPES for the financial support of this research.

Availability of Data and Materials The data supporting the findings of this study are available from the authors on reasonable request.

Declarations

Ethics Approval This manuscript has not been submitted to any previous journal of this journal. The presented work is original and has not been published elsewhere in any form or language.

Consent to Participate Not applicable.

Consent for Publication All authors have read and consented to the published version of the manuscript.

Conflict of Interest The authors declare no competing interests.

References

1. Y. Sakaguchi, S.C. Takata, Y. Kawakita, Y. Fujimura, K. Kondo, Direct observation of concentration fluctuations in Au–Si eutectic liquid by small-angle neutron scattering. J. Phys. Condens. Matter. **35**(41), 415403 (2023)
2. S. Nagireddi, B. Majumdar, S. Bonta, A.B. Diraviam, High-density bulk metallic glasses and their composites for kinetic energy penetrator applications: process, structure and properties. Trans. Indian Inst. Met. **74**, 2117–2134 (2021)
3. S.H. Lee, G.S. Hwang, Structure, energetics, and bonding of amorphous Au–Si alloys. J. Chem. Phys. **127**(22) (2007)
4. T. He, S. Chen, T. Lu, P. Zhao, W. Chen, S. Scudino, High-strength and ductile ultrafine-grained Al–Y–Ni–Co alloy for high-temperature applications. J. Alloy. Compd. **848**, 156655 (2020)
5. A. Singh, P.K. Bijalwan, A. Banerjee, M. Dutta, R.K. Mandal, J. Basu, Structures, interfaces and thermodynamic stability of nanocrystalline phases in rapidly solidified Fe-based amorphous nanocomposite ribbon, powder and coating. Mater. Charact. **186**, 111815 (2022)
6. Q. Wang, M. Chen, L. Shao, Y. Ge, P. Lin, C. Chu, B. Shen, Effects of structural relaxation on the dye degradation ability of FePC amorphous alloys. J. Non-Cryst. Solids **525**, 119671 (2019)
7. A. Kumar, R. Kumar, P. Bijalwan, M. Dutta, A. Banerjee, T. Laha, Fe-based amorphous/nanocrystalline composite coating by plasma spraying: effect of heat input on morphology, phase evolution and mechanical properties. J. Alloy. Compd. **771**, 827–837 (2019)
8. A. Inoue, Stabilization of metallic supercooled liquid and bulk amorphous alloys. Acta Mater. **48**(1), 279–306 (2000)
9. F.L. Kong, C.T. Chang, A. Inoue, E. Shalaan, F. Al-Marzouki, Fe-based amorphous soft magnetic alloys with high saturation magnetization and good bending ductility. J. Alloy. Compd. **615**, 163–166 (2014)
10. S.K. Nayak, A. Kumar, K. Sarkar, A. Pathak, A. Banerjee, T. Laha, A study on the corrosion inhibition of Fe-based amorphous/nanocrystalline coating synthesized by high-velocity oxy-fuel spraying in an extreme environment. J. Therm. Spray Technol. **28**, 1433–1447 (2019)
11. Z. Li, S. Zhou, G. Zhang, W. Zheng, Highly ductile and ultra-thick P-doped FeSiB amorphous alloys with excellent soft magnetic properties. Materials **11**(7), 1148 (2018)
12. S. Yue, H. Zhang, R. Cheng, A. Wang, Y. Dong, A. He, C.T. Liu, Magnetic and thermal stabilities of FeSiB eutectic amorphous alloys: compositional effects. J. Alloy. Compd. **776**, 833–838 (2019)
13. L. Shi, X. Hu, Y. Li, G. Yuan, K. Yao, The complementary effects of Fe and metalloids on the saturation magnetization of Fe-based amorphous alloys. Intermetallics **131**, 107116 (2021)
14. D.W. Zhang, Y. Zhang, Y.F. Cai, B.W. Zang, F. Zhao, Y.C. Wang, R. Umetsu, Z.Z. Li, X. Tong, J.T. Huo, S.L. Che, J.Q. Wang, Magnetic properties evaluation of Fe-based amorphous alloys synthesized via spark plasma sintering. J. Non-Cryst. Solids **613**, 122373 (2023)
15. D. Azuma, N. Ito, M. Ohta, Recent progress in Fe-based amorphous and nanocrystalline soft magnetic materials. J. Magn. Magn. Mater. **501**, 166373 (2020)
16. J. Guan, L. Cheng, M. Li, Microstructure and mechanical properties of Si_3N_4-Fe_3Si composites prepared by gas-pressure sintering. Materials **11**(7), 1206 (2018)
17. S. Fan, Y. Ning, X. Ma, L. Wang, J. Deng, L. Zhang, L. Cheng, Microstructure and mechanical properties of Fe–Si alloy modified C/C–SiC composites. Ceram. Int. **45**(17), 21579–21589 (2019)
18. H. Sun, C. Wang, J. Wang, M. Yu, Z. Guo, Fe-based amorphous powder cores with low core loss and high permeability fabricated using the core-shell structured magnetic flaky powders. J. Magn. Magn. Mater. **502**, 166548 (2020)
19. Y. Jiang, S. Jia, S. Chen, X. Li, L. Wang, X. Han, Theoretical prediction and experimental validation of the glass-forming ability and magnetic properties of Fe-Si-B metallic glasses from atomic structures. Materials **15**(9), 3149 (2022)
20. M.Z. Ibrahim, A.A. Sarhan, T.Y. Kuo, F. Yusof, M. Hamdi, Characterization and hardness enhancement of amorphous Fe-based metallic glass laser cladded on nickel-free stainless steel for biomedical implant application. Mater. Chem. Phys. **235**, 121745 (2019)
21. M.Z. Ibrahim, A. Halilu, A.A. Sarhan, T.Y. Kuo, F. Yusuf, M.O. Shaikh, M. Hamdi, In-vitro viability of laser cladded Fe-based metallic glass as a promising bioactive material for improved osseointegration of orthopedic implants. Med. Eng. Phys. **102**, 103782 (2022)
22. S. Lu, J. Zhang, H. Duan, Effects of B substitution for P on structure and magnetic properties of FePB amorphous alloys by first-principle investigation. Intermetallics **149**, 107674 (2022)
23. S. Ghobrial, D.W. Kirk, S.J. Thorpe, Solid state amorphization in the Ni-Nb-Y system by mechanical alloying. J. Non-Cryst. Solids **502**, 1–8 (2018)
24. K.L. Alvarez, J.M. Martín, N. Burgos, M. Ipatov, L. Domínguez, J. González, Structural and magnetic properties of amorphous and nanocrystalline Fe–Si–B–P–Nb–Cu alloys produced by gas atomization. J. Alloy. Compd. **810**, 151754 (2019)
25. C. Suryanarayana, A.A. Al-Joubori, Z. Wang, Nanostructured materials and nanocomposites by mechanical alloying: an overview. Met. Mater. Int. **28**(1), 41–53 (2022)
26. Y. Zhang, X. Li, Y. Cai, Y. Qi, S. Guo, D. Zhao, Improved hydrogen storage performances of Mg-Y-Ni-Cu alloys by melt spinning. Renew. Energy **138**, 263–271 (2019)
27. H. Liu, R. Han, H. Liu, X. Cui, M. Tang, T. Xiong, Development of hydrogen-free fully amorphous silicon oxycarbide coating by thermal organometallic chemical vapor deposition technique. J. Non-Cryst. Solids **575**, 121204 (2022)
28. H. Han, S. Jin, S. Park, Y. Kim, D. Jang, M.H. Seo, W.B. Kim, Plasma-induced oxygen vacancies in amorphous MnO_x boost catalytic performance for electrochemical CO_2 reduction. Nano Energy **79**, 105492 (2021)
29. Y. Wang, X. Zhang, B.I. Min, M. Tanaka, T. Watanabe, Synthesis of amorphous Li_3BO_3 nanoparticles as solid electrolyte for all-solid-state battery by induction thermal plasma. J. Solid State Chem. **318**, 123775 (2023)
30. B.Y. Li, A.C. Li, S. Zhao, M.A. Meyers, Amorphization by mechanical deformation. Mater. Sci. Eng. R Rep. **149**, 100673 (2022)
31. K. Edalati, H.W. Li, A. Kilmametov, R. Floriano, C. Borchers, High-pressure torsion for synthesis of high-entropy alloys. Metals **11**(8), 1263 (2021)
32. B. Mironchuk, G. Abrosimova, S. Bozhko, E. Pershina, A. Aronin, Correlation between phase transformation and surface morphology under severe plastic deformation of the $Al_{87}Ni_8La_5$ amorphous alloy. J. Non-Cryst. Solids **577**, 121279 (2022)
33. Z. Msetra, N. Khitouni, J.J. Suñol, M. Khitouni, M. Chemingui, Characterization and thermal analysis of new amorphous $Co_{60}Fe_{18}Ta_8B_{14}$ alloy produced by mechanical alloying. Mater. Lett. **292**, 129532 (2021)
34. C. Suryanarayana, Phase formation under non-equilibrium processing conditions: rapid solidification processing and mechanical alloying. J. Mater. Sci. **53**(19), 13364–13379 (2018)
35. F. Gao, S. Li, K. Li, Formation of non-equilibrium ductile solid solutions and textures in $NbCr_2$ bulks produced by mechanical milling and spark plasma sintering. J. Alloy. Compd. **826**, 154130 (2020)

36. N. Yazdian, F. Karimzadeh, M.H. Enayati, In-situ fabrication of Al_3V/Al_2O_3 nanocomposite through mechanochemical synthesis and evaluation of its mechanism. Adv. Powder Technol. **24**(1), 106–112 (2013)
37. M.G. Ozden, N.A. Morley, Laser additive manufacturing of Fe-based magnetic amorphous alloys. Magnetochemistry **7**(2), 20 (2021)
38. A. Chebli, M. Cesnek, A. Djekoun, J.J. Sunol, D. Niznansky, Synthesis, characterization and amorphization of mechanically alloyed $Fe_{75}Si_{12}Ti_6B_7$ and $Fe_{73}Si_{15}Ti_5B_7$ powders. J. Mater. Sci. **57**(26), 12600–12615 (2022)
39. L. Yan, B. Yan, Y. Jian, Fabrication of Fe-Si-B based amorphous powder cores by spark plasma sintered and their magnetic properties. Materials **15**(4), 1603 (2022)
40. F. Ahangaran, A. Hassanzadeh, S. Nouri, Surface modification of $Fe_3O_4@SiO_2$ microsphere by silane coupling agent. International Nano Letters **3**, 1–5 (2013)
41. Z.H. Wang, T. Urisu, H. Watanabe, K. Ooi, G.R. Rao, S. Nanbu, J. Maki, M. Aoyagi, Assignment of surface IR absorption spectra observed in the oxidation reactions: $2H+H_2O/Si$ (1 0 0) and H_2O+H/Si (1 0 0). Surf. Sci. **575**(3), 330–342 (2005)
42. V. Rathod, A.V. Anupama, R.V. Kumar, V.M. Jali, B. Sahoo, Correlated vibrations of the tetrahedral and octahedral complexes and splitting of the absorption bands in FTIR spectra of Li-Zn ferrites. Vib. Spectrosc. **92**, 267–272 (2017)
43. J.A. Lopez, F. González, F.A. Bonilla, G. Zambrano, M.E. Gómez, Synthesis and characterization of Fe_3O_4 magnetic nanofluid. Rev. Latinoam. Metal. Mater. **30**(1), 60–66 (2010)
44. G.H. Du, Z.L. Liu, X. Xia, Q. Chu, S.M. Zhang, Characterization and application of Fe_3O_4/SiO_2 nanocomposites. J. Sol-Gel Sci. Technol. **39**, 285–291 (2006)
45. M. Malekan, R. Rashidi, S.G. Shabestari, J. Eckert, Thermodynamic and kinetic interpretation of the glass-forming ability of Y-containing Cu-Zr-Al bulk metallic glasses. J. Non-Cryst. Solids **576**, 121266 (2022)
46. A. Radoń, P. Włodarczyk, Ł Hawełek, M. Kądziołka-Gaweł, P. Gębara, R. Nowosielski, R. Babilas, Thermodynamic approach for determining chemical composition of Fe-Co based amorphous alloys with high thermal stability and glass forming ability. J. Alloy. Compd. **763**, 141–152 (2018)
47. S.K. Wu, Y. Pan, N. Wang, T. Lu, W.J. Dai, Azo dye degradation behavior of AlFeMnTiM (M= Cr Co, Ni) high-entropy alloys. Int. J. Miner. Metall. Mater. **26**, 124–132 (2019)
48. K.Y. Hou, Q.Y. Dong, L. Su, X.Q. Zhang, Z.H. Cheng, Three-dimensional Heisenberg critical behavior in amorphous $Gd_{65}Fe_{20}Al_{15}$ and $Gd_{71}Fe_3Al_{26}$ alloys. J. Alloy. Compd. **788**, 155–162 (2019)
49. M.S. Leu, J.S. Jang, C.C. Lin, W.K. Wang, The effect of composition on the crystallization and magnetic transition of Fe-Si-B amorphous alloys. Mater. Chem. Phys. **45**(3), 275–279 (1996)
50. R.A. Parray, K. Ravichandran, Structural, thermal, electrical and magnetic properties of Fe_2CrAl FulHeusler alloy prepared by ball milling. Physica B **653**, 414665 (2023)
51. T. Rin, C. Sangwichien, R. Yamsaengsung, T. Reungpeerakul, Hydrogen generation from the hydrolysis of aluminum promoted by Ni–Li–B catalyst. Int. J. Hydrogen Energy **46**(56), 28450–28461 (2021)
52. C. Zhang, X. Zhang, S. Zhang, H. Guo, Ultrafast reductive dechlorination of carbon tetrachloride by amorphous $Fe_{78}Si_9B_{13}$ alloy. Results Phys. **14**, 102523 (2019)
53. Y. Zhu, C. Zhang, X. Liu, X. Kan, S. Feng, Q. Lv, Magnetic properties of phosphoric acid passivated Fe-Si-B amorphous magnetic powder core. Mater. Sci. Eng. B **296**, 116673 (2023)
54. K.L. Alvarez, H.A. Baghbaderani, J.M. Martín, N. Burgos, P. McCloskey, J. González, A. Masood, Novel predictive methodology of amorphisation of gas-atomised Fe-Si-B alloy powders. J. Non-Cryst. Solids **574**, 121151 (2021)
55. Y. Zhu, C. Zhang, X. Liu, X. Kan, S. Feng, Q. Lv, W. Sun, Study on the magnetic property of Fe–Si–B amorphous magnetic powder core coated with Al_2O_3/phosphoric acid–Al_2O_3 double layer. J. Mater. Sci. Mater. Electron. **34**(4), 292 (2023)
56. R.M.A. Louvier, R.A. Lopez, F.T. Fernández, P. Urban, F.G. Cuevas, Structure and size distribution of powders produced from melt-spun Fe-Si-B ribbons. Key Eng. Mater. **876**, 25–30 (2021)
57. C. Yang, Z. Liu, X. Pei, C. Jin, M. Yu, Y. Li, Magnetorheological fluid based on amorphous Fe-Si-B alloy magnetic particles. J. Intell. Mater. Syst. Struct. **33**(13), 1644–1653 (2022)

Publisher's Note Springer Nature remains neutral with regard to jurisdictional claims in published maps and institutional affiliations.

Springer Nature or its licensor (e.g. a society or other partner) holds exclusive rights to this article under a publishing agreement with the author(s) or other rightsholder(s); author self-archiving of the accepted manuscript version of this article is solely governed by the terms of such publishing agreement and applicable law.